

# Formation and Coalescence of Cosmological Supermassive Black Hole Binaries in Supermassive Star Collapse

C. Reisswig,<sup>1,\*</sup> C. D. Ott,<sup>1,2,†</sup> E. Abdikamalov,<sup>1</sup> R. Haas,<sup>1</sup> P. Mösta,<sup>1</sup> and E. Schnetter<sup>3,4,5</sup>

<sup>1</sup>*TAPIR, MC 350-17, California Institute of Technology,  
1200 E California Blvd., Pasadena, CA 91125, USA*

<sup>2</sup>*Kavli Institute for the Physics and Mathematics of the Universe (Kavli IPMU), The University of Tokyo, Kashiwa, Japan*

<sup>3</sup>*Perimeter Institute for Theoretical Physics, 31 Caroline St. N., Waterloo, ON N2L 2Y5, Canada*

<sup>4</sup>*Department of Physics, University of Guelph, 50 Stone Road East, Guelph, ON N1G 2W1, Canada*

<sup>5</sup>*Center for Computation & Technology, 216 Johnston Hall,  
Louisiana State University, Baton Rouge, LA 70803, USA*

(Dated: September 13, 2022)

We study the collapse of rapidly rotating supermassive stars that may have formed in the early Universe. By self-consistently simulating the dynamics from the onset of collapse using three-dimensional general-relativistic hydrodynamics with fully dynamical spacetime evolution, we show that seed perturbations in the progenitor can lead to the formation of a system of two high-spin supermassive black holes, which inspiral and merge under the emission of powerful gravitational radiation that could be observed at redshifts  $z \gtrsim 10$  with the DECIGO or Big Bang Observer gravitational-wave observatories, assuming supermassive stars in the mass range  $10^4 - 10^6 M_\odot$ . The remnant is rapidly spinning with dimensionless spin  $a^* = 0.9$ . The surrounding accretion disk contains  $\sim 10\%$  of the initial mass.

PACS numbers: 04.25.D-, 04.30.Db, 97.60.Bw, 02.70.Bf

The observation of supermassive black holes (SMBHs) with masses  $M \gtrsim 10^9 M_\odot$  in the early Universe at redshifts  $z \gtrsim 7$  (e.g., [1]) calls for new pathways for explaining the existence of such massive black holes when the Universe was less than 1 Gyr old (see, e.g., [2, 3] for recent reviews). Since the time available for the formation of a massive black hole via accretion from an initial seed black hole is quite short, it appears likely that the seed objects were quite massive themselves. Sufficient initial seed mass could be offered by the theoretical possibility of supermassive stars (SMSs) with masses  $10^4 - 10^6 M_\odot$ . Since SMSs can become general-relativistically unstable [4, 5], they can collapse and either form supermassive seed black holes, or, perhaps, die in powerful thermonuclear explosions with energies  $\gtrsim 10^{55}$  ergs [6–8].

A popular scenario for the formation of an SMS is the direct collapse of a primordial gas cloud in dark matter halos with virial temperatures  $\geq 10^4$  K [9–16]. The required rapid accretion rates [17] can be maintained by avoiding early fragmentation, either by isothermal collapse in the absence of  $H_2$  cooling [10, 18–22], or by turbulent accretion [14–16]. Pulsational instabilities or radiative feedback, which could limit the accretion rate, are sufficiently small to pose no problem for rapid growth [23, 24]. Since the primordial gas cloud is likely to carry substantial angular momentum, the centrifugal barrier must be overcome during the collapse of the halo gas, which could be achieved by angular momentum transfer via gravitational torques [14].

In [25], the collapse of a uniformly rotating SMS was studied in axisymmetry. Later, [26, 27] investigated the three-dimensional collapse of differentially rotating SMSs to SMBHs and found that the collapse proceeds axisym-

metrically. These studies were complemented by [28, 29], who investigated the collapse of rapidly differentially rotating SMSs with small seed perturbations that lead to fragmentation during collapse. These authors found that a small initial  $m = 1$  density perturbation grows exponentially and leads to a single, off-centered fragment that collapses to a black hole. In the case of an initial  $m = 2$  density perturbation, two orbiting and collapsing fragments form. Before the two fragments form black holes, however, a run-away collapse at the center of the SMS occurs, leading to a single black hole at the center of the star. These studies used a  $\Gamma = 4/3$   $\Gamma$ -law equation of state (EOS), which is appropriate for SMSs dominated by radiation pressure.

Recently, [6] investigated the collapse of SMSs in axisymmetry using a microphysical EOS that models the effects of radiation and electron-positron pair production. They found that above central temperatures  $\gtrsim 10^9$  K, pair creation effectively reduces the adiabatic index below  $\Gamma = 4/3$ , thus accelerating the collapse once these temperatures are reached.

In this Letter, we show that by assuming a  $\Gamma$ -law EOS with slightly reduced  $\Gamma < 4/3$ , e.g., because of pair-creation, it is possible to form a binary black hole system, provided certain small seed perturbations are present at the onset of collapse and the star is rapidly differentially rotating. The binary black hole system subsequently inspirals and merges under the emission of powerful gravitational radiation.

*Methods.* We employ general-relativistic hydrodynamics with adaptive mesh-refinement provided by the open source `EinsteinToolkit` [30, 31] using the `Llama` multipatch infrastructure [32, 33], and a modified version of

TABLE I: Black hole Christodoulou masses  $M_{\text{BH}}$  and dimensionless Kerr spin parameter  $a_{\text{BH}}^*$  for each black hole in each model. In model M2G2, we list the parameters of the inspiraling two black holes in the first two rows, and the merger remnant by the end of the simulation in the third row. We also report the disk mass  $M_{\text{disk}}$  by the end of the simulation, the measured accretion rate  $\dot{M}$ , and the radiated GW energy  $E_{\text{GW}}$ . For model M2G2, where multiple resolutions are available, we are able to provide error bars. Units are in  $c = G = M = K = 1$ , unless otherwise specified.

	M1G1	M2G1	M2G2
BH mass $M_{\text{BH}}$ [ $M$ ]	5.4	5.8	$3.0 \pm 0.1$
	-	-	$3.0 \pm 0.1$
	-	-	$5.8 \pm 0.2$
BH spin $a_{\text{BH}}^*$	0.9	0.9	$0.7 \pm 0.02$
	-	-	$0.7 \pm 0.02$
	-	-	$0.9 \pm 0.01$
bar. disk mass $M_{\text{disk}}$ [ $M$ ]	1.3	1	$0.7 \pm 0.2$
accretion rate $\dot{M}$	$1.2 \times 10^{-3}$	$2 \times 10^{-4}$	$6.7 \times 10^{-5}$
rad. GW energy $E_{\text{GW}}$ [%]	0.02	0.16	3.71

WENO5 reconstruction [30, 34]. We evolve the space-time geometry with the Z4c system [35], extract gravitational waves (GWs) at future null infinity via Cauchy-characteristic extraction [36–39], and find apparent horizons using `AHFinderDirect` [40]. We employ a  $\Gamma$ -law EOS and use an artificial low-density atmosphere ( $10^{-10}$  the central density). If not stated otherwise, all units are in  $c = G = M = K = 1$ , where  $K$  is the polytropic scale. Since our models can be rescaled to any desired mass, we report most numbers in units of mass  $M$ . For convenience, we give the conversion factors to cgs units in the Appendix.

*Initial conditions.* We consider 3 initial SMS models. Their initial data are generated via Hachisu’s self-consistent field method [41, 42], which requires as input the central density  $\rho_c$  of the star, and a polar-to-equatorial axes ratio  $r_p/r_e$  between 0 and 1 together with a dimensionless parameter  $A$  to set the degree of differential rotation. All models are set up as marginally stable  $\Gamma = 4/3$  polytropes with scale  $K = 1$ . In every case, the central density is set to  $\rho_c = 3.38 \times 10^{-6} M^{-2}$ , the axes ratio is set to  $r_p/r_e = 0.24$ , and the differential rotation parameter is set to  $A = 1/3$ . With these input parameters, the baryonic mass of the star becomes  $M_{*,\text{bar}} = 7.0527M$ , the gravitational mass of the star is  $M_{*,\text{ADM}} = 7.0037M$ , and the angular momentum becomes  $J = 52.206 M^{-2}$ , which corresponds to a dimensionless Kerr spin parameter of  $a^* \equiv J/M^2 = 1.0643$ . The resulting equatorial radius is  $r_e = 82M$ . Due to the rapid rotation, the star has quasi-toroidal shape (its density maximum is off-center). The various models differ by the type of initial perturbation that is applied and by how the collapse is induced. In two models, M1G1 and M2G1, the collapse is accelerated by reducing the polytropic scale  $K$  by  $10^{-3}$  initially. During evolution, the two mod-

els use an adiabatic index  $\Gamma = 4/3$ . In model M2G2, the collapse is triggered by reducing  $\Gamma = 4/3$  to  $\Gamma = 1.33$ . To induce fragmentation during collapse, we apply a density perturbation to the initial configuration. The perturbation is given by  $\rho_{\text{ini}} \rightarrow \rho_{\text{ini}}(1 + A_m r \sin(m\phi))$ , where  $m > 0$  is an integer,  $A_m$  is the perturbation amplitude,  $r$  a cylindrical coordinate radius, and  $\phi$  a cylindrical coordinate angle. This perturbation offers reasonable overlap with the corresponding quasinormal modes of the star. In model M1G1, we apply a  $m = 1$  perturbation, and in models M2G1 and M2G2, we apply a  $m = 2$  perturbation. We use a perturbation amplitude of  $A_m = 10^{-3}/r_e \approx 1.22 \times 10^{-5}$ .

*Grid setup.* We use the multiblock grid setup described in [32]: A central Cartesian grid is surrounded by six spherical “inflated-cube” grids. Their interface is located at radius  $R_s = 240M$ , and the outer boundary is at  $R_b = 4000M$ . The central Cartesian grid is capable of 2:1 mesh refinement. We use 2 additional finer grids, one covering the entire star, the other covering the high density torus. We perform simulations using three resolutions labeled by  $r0$ ,  $r1$ , and  $r2$ . In our baseline resolution  $r1$ , the initially finest level has a resolution of  $\Delta x = 0.4M$ . During evolution, we track each forming fragment with a moving refinement center. While a fragment collapses, we progressively add an additional refinement level every time the fragment’s central density increases by another order of magnitude. In total, we switch on up to 3 additional refinement levels for each fragment until a black hole forms. The finest level has a resolution of  $\Delta x = 0.05M$ . The outer spherical grids have radial spacing  $\Delta r = 3.2M$  and use  $N_{\text{ang}} = 21$  cells per patch and angular direction, which corresponds to an angular resolution of  $\simeq 4.3^\circ$ . The other resolutions  $r0$  and  $r2$  have 25% decreased and 25% increased resolution. See the Appendix for demonstration of numerical convergence.

*Dynamics.* Following the initial pressure reduction, either by reducing  $K$  or by reducing  $\Gamma$ , the rapidly rotating SMSs undergo accelerated collapse. Depending on the initial density perturbation, the stars fragment, and collapse accelerates in the fragments. Model M1G1, due to its  $m = 1$  initial density perturbation, forms a single off-centered fragment which orbits around the star’s center while collapsing. At  $T = 2145M$ , an apparent horizon emerges around the center of the fragment. Model M2G1, due to its  $m = 2$  initial density perturbation, forms two orbiting fragments that slowly inspiral and collapse. After  $T \simeq 2335M$ , when the two fragments are still well separated, run-away collapse occurs at the center of the star, leading to a rapid increase of the central density. A single apparent horizon emerges around the center of the SMS at  $T = 2470M$ . Models M1G1 and M2G1 were both considered in [28, 29], and we confirm their findings, though we are able to continue the evolution well beyond the appearance of an apparent horizon. We stop

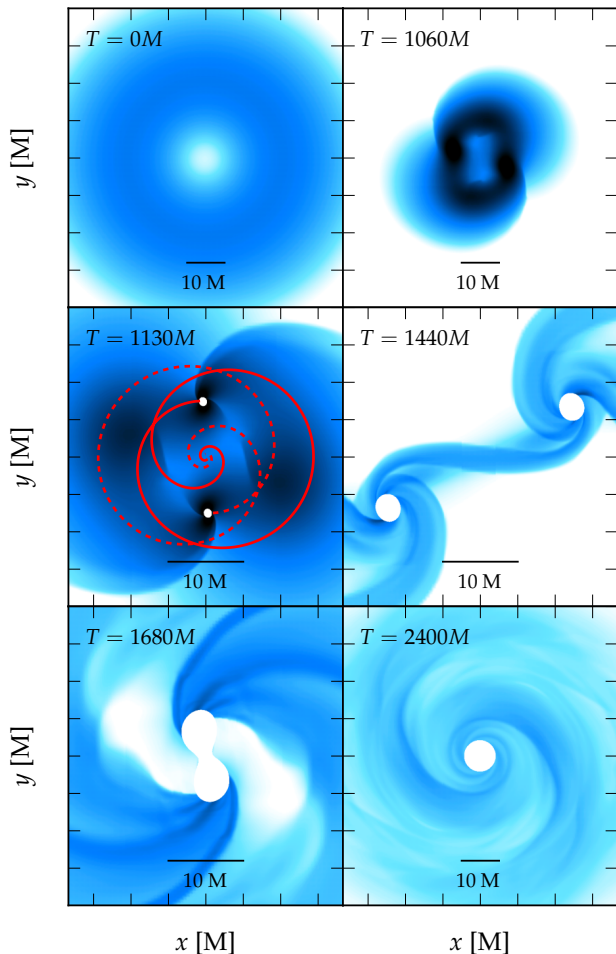


FIG. 1: Snapshots of a slice of the equatorial density distribution of model M2G2. Dark colors indicate high density, light colors indicate low density. The logarithmic density colormap ranges from  $10^{-7}M^{-2}$  (white) to  $10^{-3}M^{-2}$  (black). In the bottom two panels, the colormap is rescaled to the range  $[10^{-8}M^{-2}, 10^{-4}M^{-2}]$  for the sake of presentation. The upper two and the bottom right panels show an extent of  $\pm 40M$ , while the remaining panels show an extent of  $\pm 20M$ .

the simulation at  $T \simeq 3500M$ . Model M2G2 initially follows qualitatively the evolution of model M2G1. Due to its softer  $\Gamma$ , however, the two fragments collapse much faster, forming a pair of two black holes. In Fig. 1, we show the equatorial density distribution of model M2G2 at various stages during the evolution. The upper left panel shows the inner  $80M$  of the initial density distribution. The toroidal high density ring is clearly visible. The upper right panel shows a snapshot during collapse. Due to the initial density perturbation, a strong  $m = 2$  deformation arises with two inspiraling high-density fragments. The center-left panel shows the density distribution at time  $T = 1130M$  when an apparent horizon appears within each of the two still well separated fragments. The apparent horizons are indicated by white circular regions. For the purpose of visualization, they

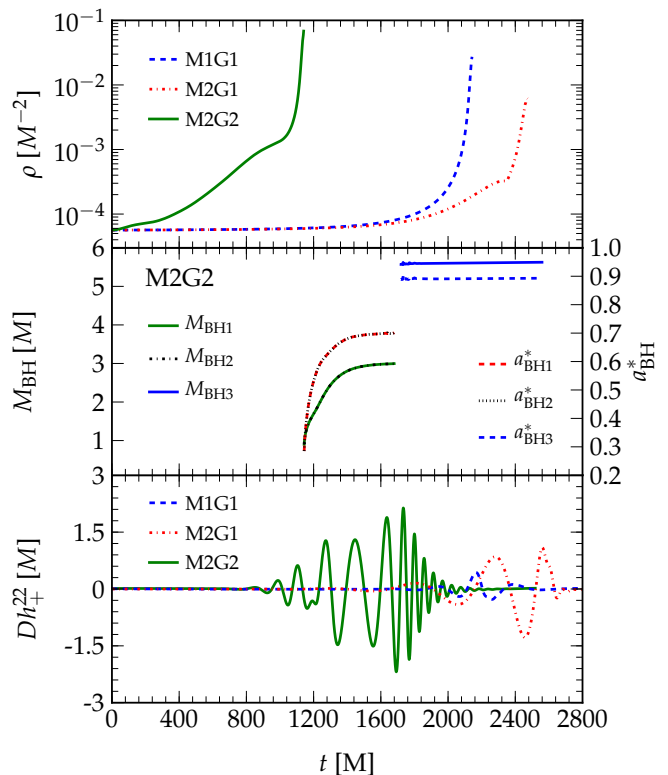


FIG. 2: *Top panel*: Evolution of the maximum density for all models. *Center panel*: Spin and mass evolution of all three black hole horizons of model M2G2. *Lower panel*:  $(\ell, m) = (2, 2)$  spherical harmonic mode of the “+” polarization of the emitted gravitational radiation rescaled by distance  $D$ .

are approximated by the lapse gauge function  $\alpha$  (with the region  $\alpha \leq 0.19$  closely resembling their coordinate shapes). The two nascent black holes have identical mass and spin. Initially, they have a coordinate separation  $D = 13.2M$ , a Christodoulou mass  $M_{\text{BH}} = 0.899M$ , and dimensionless spin  $a_{\text{BH}}^* = 0.286$ . Their spin axes are both aligned with the orbital angular momentum. Transfer of angular momentum from the differentially rotating torus onto the black holes via accretion leads to an outwards spiraling motion until the two black holes reach a separation  $D = 24.7M$ . From there, they start to inspiral driven by GW emission and merge after  $\sim 1.5$  orbits. The tracks of the black holes are indicated by red (solid and dashed) lines in the center-left panel of Fig. 1. In the center-right panel, the black holes have completed close to one orbit. Around each black hole, material is dragged and accreted, forming spiral patterns. During inspiral, while further accreting material, each of the two black holes grows to a mass  $M_{\text{BH}} = 3 \pm 0.1M$  and dimensionless spin parameter  $a_{\text{BH}}^* = 0.7 \pm 0.02$  just before merger (center panel of Fig. 2). In the bottom left panel of Fig. 1, the two black holes are about to merge at time  $T = 1680M$ , and a common apparent horizon appears. The bottom-right panel shows the sit-

uation at the end of the simulation after the system has settled to a quasi-stationary state. The merger remnant has a Christodoulou mass  $M_{\text{BH}} = 5.8 \pm 0.2M$ , and dimensionless spin  $a_{\text{BH}}^* = 0.9 \pm 0.01$ . The surrounding accretion disk quickly settles to a baryonic mass  $M_{\text{disk}} = 0.7 \pm 0.2M$ .

*GW emission.* All models emit GWs during collapse and while the fragments form and orbit around the center of the star. The dominant radiated GW mode for all models is  $(\ell, m) = (2, 2)$ . In models with  $m = 2$  deformation, the emission is particularly strong. The strongest emission is generated by model M2G2 due to the two inspiraling and merging SMBHs. In Fig. 2, we show the evolution of the maximum density as well as the  $(\ell, m) = (2, 2)$  mode of the “+” polarization of the emitted GW signal. As the maximum density increases, the oscillatory GW signal rises in amplitude. Following BH formation, a GW ring-down signal is emitted in models M1G1 and M2G1. In model M2G2, following BH formation, we obtain a binary black hole inspiral signal which increases in frequency and amplitude towards merger. Following merger, the remnant emits ring-down GWs. The entire GW signal is in the dHz frequency band for  $M_* \sim 10^4 M_\odot$  SMSs, and in the mHz band for  $M_* \sim 10^6 M_\odot$  SMSs.

Using modes up to  $\ell = 8$ , we compute the radiated energy emitted in GWs. In model M1G1, 0.02% of the initial gravitational mass  $M_{*,\text{ADM}}$  is radiated in GWs, 0.16% is radiated in model M2G1, and 3.71% is radiated in model M2G2 (see Table I). We compute the detectabilities by the proposed space-borne eLISA, DECIGO, and Big Bang Observer GW observatories [43–45] over a range of redshifts  $z \in [5, 100]$  and source masses  $M_* \in [10^4 M_\odot, 10^6 M_\odot]$ . Assuming a  $\Lambda$ CDM cosmology with parameters measured by the Planck mission [46], we compute the luminosity distance  $D(z)$  and redshifted mass  $(1+z)M_*$  for a given redshift  $z$ . The optimal and angle-averaged signal-to-noise ratios (SNRs) (e.g. [47, 48]) can then be obtained from the Fourier-transformed angle-dependent GW signal  $\tilde{h}(\theta, \phi)$  using the corresponding theoretical GW observatory sensitivity curves [43, 45, 49], the luminosity  $D(z)$  and corresponding redshifted mass  $(1+z)M_*$ . Assuming a minimum SNR of 8 for detection, we obtain a maximum redshift of  $z \simeq 25$  for a  $M_* = 10^4 M_\odot$  SMS in DECIGO and the Big Bang Observer, provided the system’s spin axis is pointing towards Earth  $((\theta, \phi) = (0, 0))$ . Both detectors are limited by the white dwarf confusion noise at low frequencies (e.g. [49]) and have very similar sensitivity for the considered mass range. Higher mass SMSs are detectable only out to smaller redshifts. For a  $M_* = 10^6 M_\odot$  SMS, we obtain a maximum redshift  $z \simeq 16$  for detection. By assuming a random orientation of the spin axis, we obtain a mean GW detectability out to  $z \simeq 23$  for low-mass SMSs, and  $z \simeq 13$  for high-mass SMSs. In eLISA, the signal is barely detectable at  $z \simeq 6$ , which is outside the

relevant range of redshifts  $z \gtrsim 10$  at which SMSs are anticipated to exist.

*Discussion.* We have self-consistently simulated the collapse of SMSs using 3 + 1 general-relativistic hydrodynamics with approximation-free dynamical spacetime evolution. We have shown that it is possible to form a coalescing binary SMBH system in SMS collapse provided the following conditions are realized: (i) the SMS must be rapidly differentially rotating, (ii) the gas pressure must be reduced by a process effectively lowering  $\Gamma < 4/3$ , (iii) a small initial  $m = 2$  density perturbation must be present. The first condition may easily be met since collapsing primordial gas clouds are likely to carry substantial angular momentum. If an SMS forms, it is thus expected to rotate rapidly. The second condition is motivated by recent simulations of SMSs using a microphysical EOS [6]. At sufficiently high central temperatures  $\gtrsim 10^9$  K encountered during the collapse, the effective  $\Gamma$  is lowered due to electron-positron pair-production. Even if the collapse is triggered purely gravitationally, the temperature eventually increases, causing an effective decrease in  $\Gamma$ . We find that lowering  $\Gamma$  by not more than 0.25% accelerates the collapse sufficiently to form a pair of two SMBHs. Finally, condition (iii) does not seem unlikely, since recent simulations of the direct collapse of primordial gas clouds [14] find that central supermassive objects that may lead to SMSs form  $m = 2$  structures. In any case, small seed perturbations are likely to be present at the onset of collapse. For our SMS model, the  $m = 1$  and  $m = 2$  modes have the fastest and very similar growth rates [28, 29]. Therefore, even a tiny  $m = 2$  bias in an initially randomly perturbed model may result in fast growth of the  $m = 2$  mode and formation of two fragments. A detailed analysis of this will be subject of future work.

If  $m = 2$  fragmentation and binary SMBH formation occurs in SMS collapse, the coalescence of the SMBH binary will result in a unique GW signal that can be detected at redshifts  $z \gtrsim 10$  with DECIGO and Big Bang Observer for SMSs in the mass range  $10^4 - 10^6 M_\odot$ . If detected and identified, such a signal would confirm the existence of SMSs and could potentially inform us about their rotation and thermodynamics. Moreover, the interaction between matter and the binary SMBHs will likely result in an electromagnetic signature, the details of which will need to be established by future work.

We acknowledge helpful discussions with Volker Bromm, Sterl Phinney, Michele Vallisneri and members of our Simulating eXtreme Spacetimes (SXS) collaboration (<http://www.black-holes.org>). This research is partially supported by NSF grant nos. PHY-1151197, AST-1212170, PHY-1212460, and OCI-0905046, by the Alfred P. Sloan Foundation, and by the Sherman Fairchild Foundation. CR acknowledges support by NASA through Einstein Postdoctoral Fellowship grant number PF2-130099 awarded by the Chandra X-ray cen-

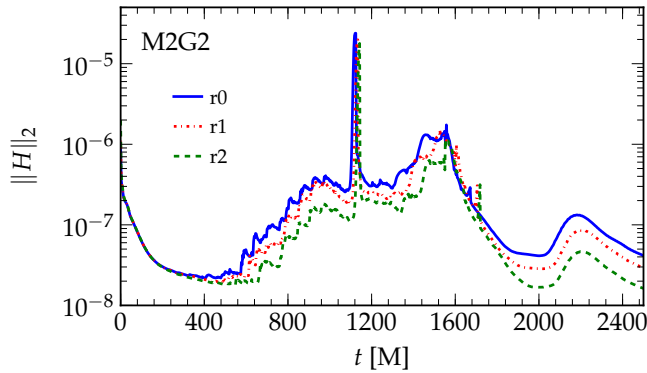


FIG. 3: Convergence of the  $L_2$ -norm of the Hamiltonian constraint  $\|H\|_2$  of model *M2G2* for the low  $r0$ , medium  $r1$ , and high resolution  $r2$  (not rescaled). As the resolution is increased, the error decreases with a convergence rate between first and second-order as expected. The peaks occur when the black holes form, and when the black hole interior is not yet excluded from the calculation of the  $L_2$ -norm.

ter, which is operated by the Smithsonian Astrophysical Observatory for NASA under contract NAS8-03060. RH acknowledges support by the Natural Sciences and Engineering Council of Canada. The simulations were performed on the Caltech compute cluster *Zwicky* (NSF MRI award No. PHY-0960291), on supercomputers of the NSF XSEDE network under computer time allocation TG-PHY100033, on machines of the Louisiana Optical Network Initiative under grant loni\_numrel08, and at the National Energy Research Scientific Computing Center (NERSC), which is supported by the Office of Science of the US Department of Energy under contract DE-AC02-05CH11231.

### Numerical Convergence

We show numerical convergence of our results by considering the Hamiltonian constraint  $H$ .  $H = 0$  is one of the four elliptic constraint equations which arise from the 3+1 ADM decomposition of the Einstein equations (e.g. [50]). Any solution to the Einstein equation must satisfy these constraints. At the continuum level, if they are satisfied initially, they are automatically satisfied at all times. During a numerical evolution, however, numerical error can lead to constraint violations. As the resolution is increased, the constraints must converge to zero at the expected order of accuracy inherent to the numerical scheme.

As detailed in [32], the overall accuracy of our simulations is limited by the finite-volume hydrodynamics scheme, which is second-order accurate in regions where the fluid flow is smooth, and reduces to first order near shocks and discontinuities. Thus, we expect between first and second-order convergence. We note that the we

TABLE II: Conversion factors for 1 solar mass  $M_\odot$  in code units  $c = G = M = K = 1$  to cgs units.

Quantity	code	cgs
Mass $M$	$M$	$1.9891 \times 10^{33} (M/M_\odot)$ g
Length $L$	$M$	$1.4771 \times 10^5 (M/M_\odot)$ cm
Time $T$	$M$	$4.9271 \times 10^{-6} (M/M_\odot)$ sec
Density $\rho$	$M^{-2}$	$6.1716 \times 10^{17} (M_\odot/M)^2$ g cm $^{-3}$

evolve the spacetime geometry with a fourth-order finite-difference scheme [32], but the overall error is dominated by the fluid evolution.

In Fig. 3, we show the  $L_2$ -norm of the Hamiltonian constraint  $\|H\|_2$  of model *M2G2* (which forms a pair of black holes) for three resolutions labeled by  $r0$ ,  $r1$ , and  $r2$ . The coarse resolution,  $r0$ , has 25% reduced resolution compared to baseline resolution  $r1$ , and  $r2$  has 25% increased resolution. The  $L_2$ -norm is taken over the entire domain, excluding the interior of the black hole horizons. With increasing resolution,  $\|H\|_2$  decreases with a convergence rate consistent with first and second order as expected. More specifically, we find that  $\|H\|_2^{r2} \leq 1.25 \|H\|_2^{r1} \leq 1.25 \|H\|_2^{r0}$ . We note that the numerical evolution is initially non-convergent for the first  $t \leq 250M$  due to the non-constraint preserving application of an initial density perturbation.

### Conversion of Units

For convenience, we provide the conversion factors from code units  $c = G = M = K = 1$  to cgs units in Table II. As an example for a  $M = 10^6 M_\odot$  star, a code unit time of  $T = 1M$  corresponds to a physical time  $t \simeq 4.93$  sec, the initial stellar equatorial radius  $r_e = 80M$  corresponds to  $\simeq 1.2 \times 10^8$  km  $\simeq 0.8$  AU, and the initial central density  $\rho_c = 3.38 \times 10^{-6} M^{-2}$  is  $\simeq 2.1$  g cm $^{-3}$ .

\* Einstein Fellow; Electronic address: reisswig@tapir.caltech.edu

† Alfred P. Sloan Research Fellow

- [1] D. J. Mortlock, S. J. Warren, B. P. Venemans, M. Patel, P. C. Hewett, et al., *Nature* **474**, 616 (2011).
- [2] M. Volonteri and J. Bellovary, *Rept.Prog.Phys.* **75**, 124901 (2012).
- [3] X. Fan, *New Astron. Rev.* **50**, 665 (2006).
- [4] S. L. Shapiro and S. A. Teukolsky, *Astrophys. J. Lett.* **234**, L177 (1979).
- [5] T. W. Baumgarte and S. L. Shapiro, *Astrophys. J.* **526**, 941 (1999).
- [6] P. J. Montero, H.-T. Janka, and E. Müller, *Astrophys. J.* **749**, 37 (2012).
- [7] D. J. Whalen, A. Heger, K.-J. Chen, W. Even, C. L. Fryer, M. Stiavelli, H. Xu, and C. C. Jøgerst,

- arXiv:1211.1815 (2012).
- [8] J. L. Johnson, D. J. Whalen, W. Even, C. L. Fryer, A. Heger, J. Smidt, and K.-J. Chen, arXiv:1304.4601 (2013).
- [9] S. P. Oh and Z. Haiman, *Astrophys. J.* **569**, 558 (2002).
- [10] V. Bromm and A. Loeb, *Astrophys. J.* **596**, 34 (2003).
- [11] M. C. Begelman, M. Volonteri, and M. J. Rees, *Mon. Not. Roy. Astron. Soc.* **370**, 289 (2006).
- [12] D. R. G. Schleicher, M. Spaans, and S. C. O. Glover, *Astrophys. J. Lett.* **712**, L69 (2010).
- [13] B. Agarwal, S. Khochfar, J. L. Johnson, E. Neistein, C. Dalla Vecchia, and M. Livio, *Mon. Not. Roy. Astron. Soc.* **425**, 2854 (2012).
- [14] J.-H. Choi, I. Shlosman, and M. C. Begelman, arXiv:1304.1369 (2013).
- [15] M. A. Latif, D. R. G. Schleicher, W. Schmidt, and J. Niemeyer, *Mon. Not. Roy. Astron. Soc.* **430**, 588 (2013).
- [16] M. A. Latif, D. R. G. Schleicher, W. Schmidt, and J. Niemeyer, arXiv:1304.0962 (2013).
- [17] M. C. Begelman, *Mon. Not. Roy. Astron. Soc.* **402**, 673 (2010).
- [18] M. Spaans and J. Silk, *Astrophys. J.* **652**, 902 (2006).
- [19] J. H. Wise, M. J. Turk, and T. Abel, *Astrophys. J.* **682**, 745 (2008).
- [20] J. A. Regan and M. G. Haehnelt, *Mon. Not. Roy. Astron. Soc.* **393**, 858 (2009).
- [21] M. A. Latif, S. Zaroubi, and M. Spaans, *Mon. Not. Roy. Astron. Soc.* **411**, 1659 (2011).
- [22] J. L. Johnson, S. Khochfar, T. H. Greif, and F. Durier, *Mon. Not. Roy. Astron. Soc.* **410**, 919 (2011).
- [23] K. Inayoshi, T. Hosokawa, and K. Omukai, arXiv:1302.6065 (2013).
- [24] T. Hosokawa, K. Omukai, and H. W. Yorke, *Astrophys. J.* **756**, 93 (2012).
- [25] M. Shibata and S. L. Shapiro, *Astrophys. J. Lett.* **572**, L39 (2002).
- [26] M. Saijo, *Astrophys. J.* **615**, 866 (2004).
- [27] M. Saijo and I. Hawke, *Phys. Rev. D.* **80**, 064001 (2009).
- [28] B. Zink, N. Stergioulas, I. Hawke, C. D. Ott, E. Schnetter, and E. Müller, *Physical Review Letters* **96**, 161101 (2006).
- [29] B. Zink, N. Stergioulas, I. Hawke, C. D. Ott, E. Schnetter, and E. Müller, *Phys. Rev. D.* **76**, 024019 (2007).
- [30] P. Mösta, B. Mundim, J. Faber, R. Haas, S. Noble, T. Bode, F. Löffler, C. D. Ott, C. Reisswig, and E. Schnetter, arXiv:1304.5544 (2013).
- [31] F. Löffler, J. Faber, E. Bentivegna, T. Bode, P. Diener, R. Haas, I. Hinder, B. C. Mundim, C. D. Ott, E. Schnetter, et al., *Class. Quantum Grav.* **29**, 115001 (2012).
- [32] C. Reisswig, R. Haas, C. D. Ott, E. Abdikamalov, P. Moesta, D. Pollney, and E. Schnetter, *Phys. Rev. D.* **87**, 064023 (2013).
- [33] D. Pollney, C. Reisswig, E. Schnetter, N. Dorband, and P. Diener, *Phys. Rev. D.* **83**, 044045 (2011).
- [34] A. Tchekhovskoy, J. C. McKinney, and R. Narayan, *Mon. Not. Roy. Astron. Soc.* **379**, 469 (2007).
- [35] D. Hilditch, S. Bernuzzi, M. Thierfelder, Z. Cao, W. Tichy, and B. Bruegmann, arXiv:1212.2901 (2012).
- [36] C. Reisswig, N. T. Bishop, D. Pollney, and B. Szilagyi, *Phys. Rev. Lett.* **103**, 221101 (2009).
- [37] C. Reisswig, N. T. Bishop, D. Pollney, and B. Szilágyi, *Class. Quantum Grav.* **27**, 075014 (2010).
- [38] C. Reisswig, C. D. Ott, U. Sperhake, and E. Schnetter, *Phys. Rev. D.* **83**, 064008 (2011).
- [39] C. Reisswig and D. Pollney, *Class. Quantum Grav.* **28**, 195015 (2011).
- [40] J. Thornburg, *Class. Quant. Grav.* **21**, 743 (2004).
- [41] H. Komatsu, Y. Eriguchi, and I. Hachisu, *Mon. Not. Roy. Astron. Soc.* **239**, 153 (1989).
- [42] N. Stergioulas and J. L. Friedman, *Astrophys. J.* **444**, 306 (1995).
- [43] O. Jennrich et al., Tech. Rep. ESA/SRE(2011)19, European Space Agency (2011).
- [44] S. Kawamura, M. Ando, N. Seto, S. Sato, T. Nakamura, K. Tsubono, N. Kanda, T. Tanaka, J. Yokoyama, I. Funaki, et al., *Classical and Quantum Gravity* **28**, 094011 (2011).
- [45] C. Cutler and D. E. Holz, *Phys. Rev. D.* **80**, 104009 (2009).
- [46] P. Ade et al. (Planck Collaboration), arXiv:1303.5076 (2013).
- [47] É. É. Flanagan and S. A. Hughes, *Phys. Rev. D* **57**, 4535 (1998).
- [48] C. Reisswig, S. Husa, L. Rezzolla, E. N. Dorband, D. Pollney, and J. Seiler, *Phys. Rev. D.* **80**, 124026 (2009).
- [49] A. Nishizawa, K. Yagi, A. Taruya, and T. Tanaka, *Phys. Rev. D.* **85**, 044047 (2012).
- [50] M. Alcubierre and M. D. Mendez, *Gen.Rel.Grav.* **43**, 2769 (2011).